

SUPPLEMENTARY INFORMATION FOR

Unraveling spin-orbit torque induced multistate magnetization switching in  
Co/Gd ferrimagnetic multilayers for physically unclonable functions

Caiyun Li,<sup>†a</sup> Renyou Xu,<sup>†a</sup> Yuqi Duan,<sup>a</sup> Xiuye Zhang,<sup>a</sup> Daoqian Zhu,<sup>\*a,b</sup> Ao Du,<sup>a</sup> Zhiyang Peng,<sup>a</sup> Shiqi Wang,<sup>a</sup> Kewen Shi,<sup>a,b</sup> Weisheng Zhao<sup>\*a,b</sup>

*a. Fert Beijing Institute, School of Integrated Circuit Science and Engineering, Beihang University, Beijing 100191, China.*

*b. National Key Laboratory of Spintronics, Hangzhou International Innovation Institute, Beihang University, Hangzhou 311115, China.*

<sup>†</sup> Equal contribution

\* Corresponding author: daoqian\_zhu@buaa.edu.cn; weisheng.zhao@buaa.edu.cn

**S1: Saturation magnetization of [Co/Gd]<sub>n</sub> and [Co/Gd]<sub>L</sub>/CFB stacks**

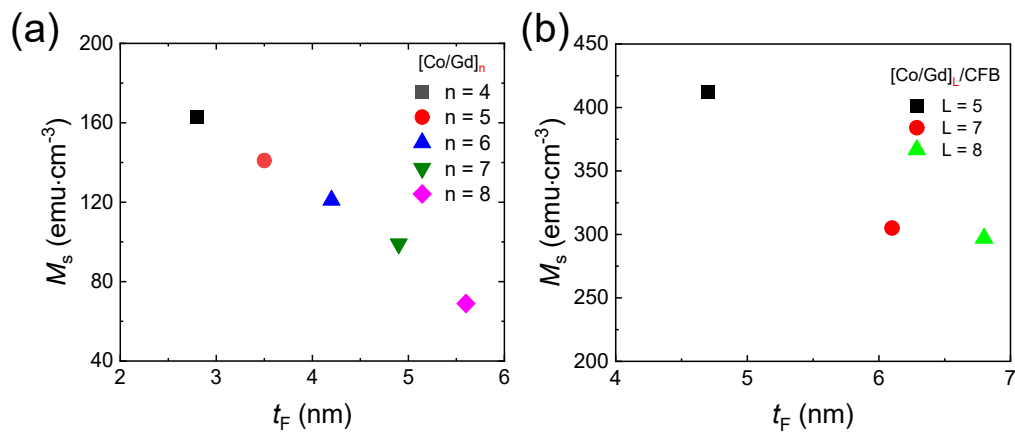


Fig. S1. Saturation magnetization of (a)  $[Co/Gd]_n$  and (b)  $[Co/Gd]_L/CFB$  stacks.

## S2: Temperature-dependent AHE and SOT-driven multistate switching in samples with $n = 6, 8$ .

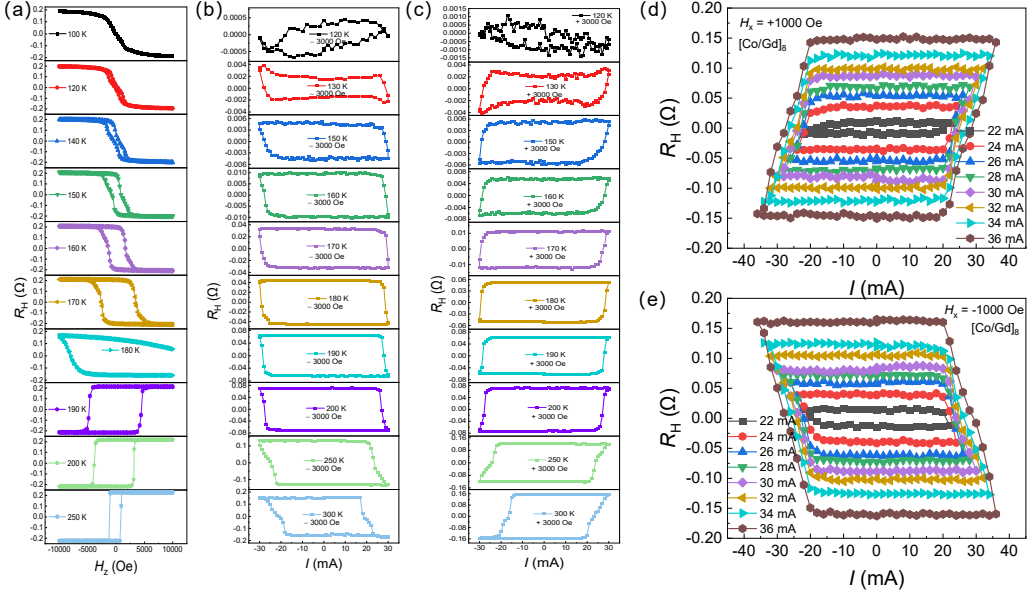


Fig. S2. (a) The  $R_H$  -  $H_z$  loops for one  $[Co/Gd]_6$  Hall bar device varies from 100 K to 250 K. The  $R_H \sim I$  loops of  $[Co/Gd]_6$  Hall bar device driven by pulsed currents ranging from 120 K to 300 K with (b) a negative assisting field or (c) a positive assisting field. (d) - (e)  $R_H \sim I$  loops in  $[Co/Gd]_8$  samples driven by pulsed currents ranging from 22 to 36 mA with positive and negative assist field  $H_x$ , respectively.

## S3: Magnetic field driven hysteresis loops when varying the polar angle

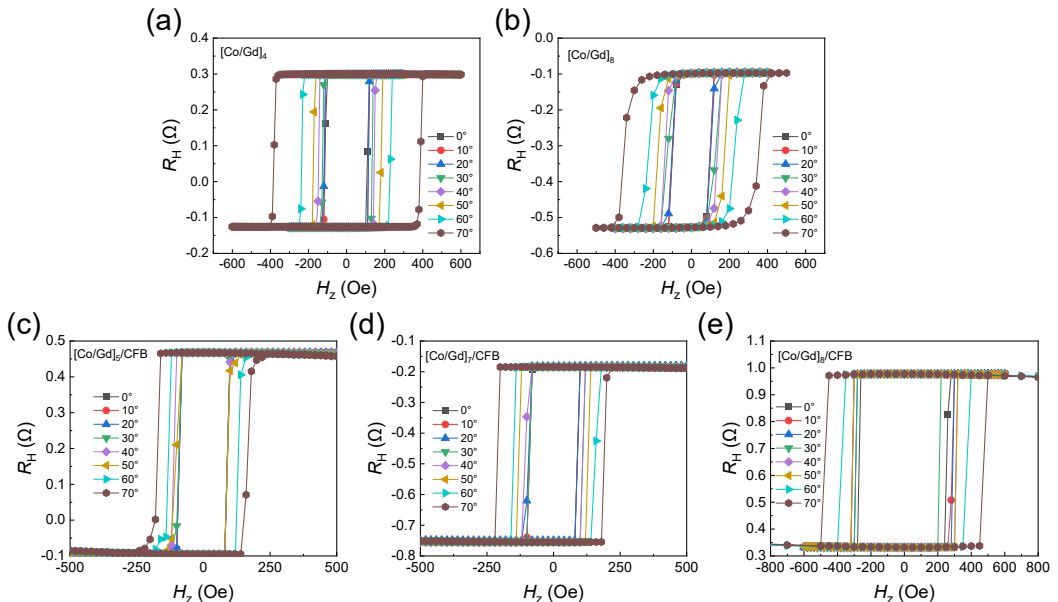


Fig. S3.  $R_H$  -  $H_z$  loops as a function of  $\theta_H$  in (a) - (b)  $[Co/Gd]_n$  ( $n = 4, 8$ ) and (c) - (f)  $[Co/Gd]_L/CFB$  ( $L = 1$ ).

5, 7, 8).

#### S4: The simulation of current density distribution in Hall bar devices

We built the Hall bar device geometry with a 70- $\mu\text{m}$  length and 10- $\mu\text{m}$  width to match an actual cross-shaped Hall bar. The normalized current density distribution results, presented in Fig. S4, indicate that the current density near the electrode is 1.4 times larger than that at the Hall cross area.

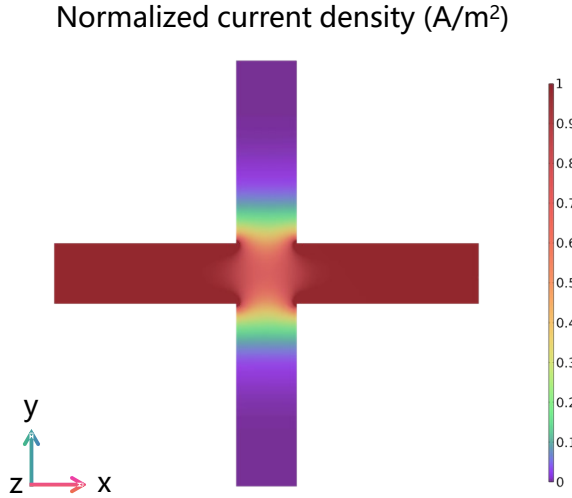


Fig. S4. The normalized current density distribution in Hall bar device.

#### S5: Micromagnetic simulations

Micromagnetic simulations were performed on the open-source platform Mumax3 to support the multistate switching mechanism [1]. To introduce the pinning effect, the simulated region with a lateral dimension of 1000 nm  $\times$  1000 nm was divided into grains with an average size of 60 nm using a Voronoi tessellation. In each grain, the direction of easy axis ( $\theta, \varphi$ ) was varied, where  $\theta$  and  $\varphi$  were randomly distributed on a scale of 5 degrees and 360 degrees, respectively. In addition, the effective perpendicular anisotropy in each grain  $B_{k,i}$  was set as  $B_{k,i} = B_k + \Delta B_k$ , with  $\Delta B_k$  randomly distributed on a scale of  $\pm \delta B_k$ . Only damping-like SOT was considered. The simulation parameters are: perpendicular anisotropy field  $B_k = 0.4$  T, saturation magnetization  $M_s = 300$  KA $\cdot$ m $^{-1}$ , Gilbert damping constant  $\alpha = 0.1$ , spin Hall angle  $\theta_{\text{SH}} = 0.2$ , exchange stiffness  $A_{\text{ex}} = 13$  pJ $\cdot$ m $^{-1}$ , thickness  $t_F = 4$  nm. The simulated region has a dimension of 1000 nm  $\times$  1000 nm  $\times$  4 nm and is divided into grains with an average size of 60 nm

by a Voronoi tessellation [1]. The cell size in the simulation is  $3.90 \text{ nm} \times 3.90 \text{ nm} \times 4 \text{ nm}$ . The exchange coupling between adjacent grains is reduced by 90 % to introduce the pinning effect. We treat the ferrimagnets as a ferromagnet with reduced  $M_s$  for simplicity, but we note that the basic picture for the current-induced multistate switching can be captured.

We initialized the magnetization at  $-z$  direction and then swept the SOT current density  $J_{\text{SOT}}$  with a step of  $20 \text{ MA} \cdot \text{cm}^{-2}$  in the presence of a magnetic field of  $60 \text{ mT}$  along  $+x$  direction. At each  $J_{\text{SOT}}$ , the current pulse lasted for  $10 \text{ ns}$  and then the system was relaxed for  $10 \text{ ns}$ . Fig. S5(a) shows the simulated SOT-induced switching loop with  $\delta$  increasing from 10 % to 40 %. Clearly, the multistate switching behavior gradually becomes significant as the pinning effect is enhanced. Fig. S5(b) - 5(e) show the corresponding snapshots when  $J_{\text{SOT}}$  increases from  $140$  to  $240 \text{ MA} \cdot \text{cm}^{-2}$ , where stable intermedia states can be clearly observed for a large  $\delta$ . Our simulations indicate that multistate switching could also be expected in materials other than ferrimagnets as long as strong pinning effects can be introduced, which provides insight to engineer multistate switching in typical ferromagnets.

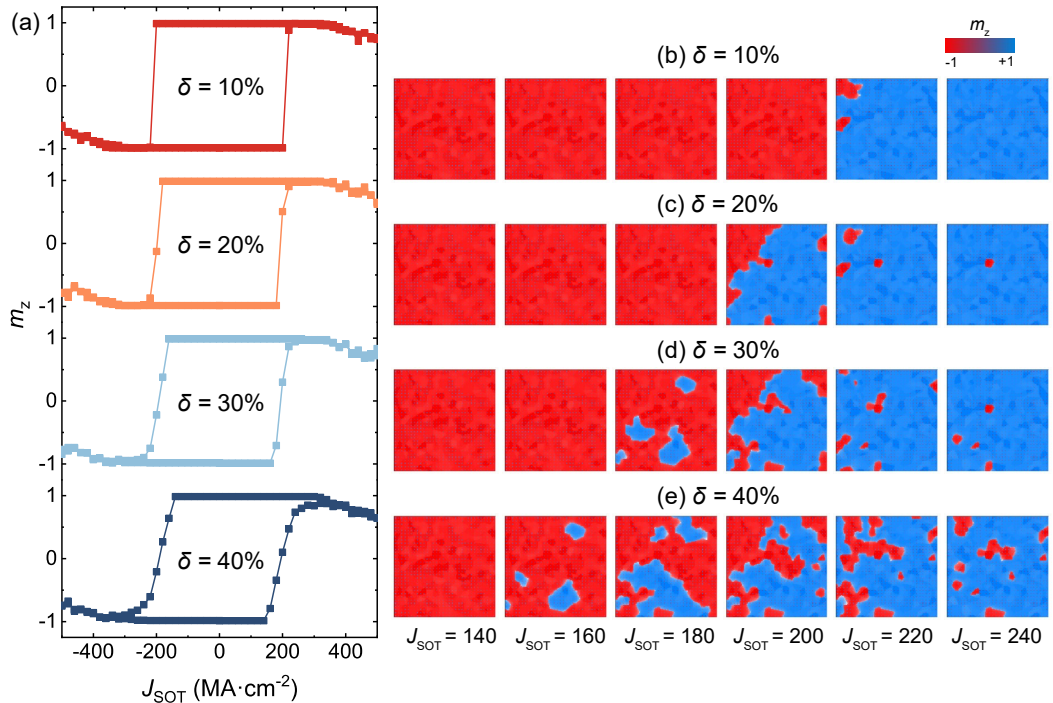


Fig. S5. (a) SOT current-induced switching loops with  $\delta$  increasing from 10 % to 40 %. (b) - (e) Corresponding magnetization snapshots when increasing  $J_{\text{SOT}}$  from  $140$  to  $240 \text{ MA} \cdot \text{cm}^{-2}$ .

## S6: The Hall bar array for PUF measurements

We fabricated a Hall bar array for a conceptual PUF (Physical Unclonable Function) chip design, consisting of 150 units, as shown in Fig. S6. This array includes 150 Hall bar devices as a precautionary measure to prevent incomplete array data in the event that some devices are damaged during testing. However, only 100 of these Hall bar devices were selected to form a  $10 \times 10$  PUF array. This selection ensures a robust and reliable PUF system while providing sufficient redundancy to account for potential defects or failures during the fabrication and testing processes. The remaining 50 Hall bar devices serve as backups or can be utilized for additional testing and characterization to further enhance the performance and reliability of the PUF chip design.

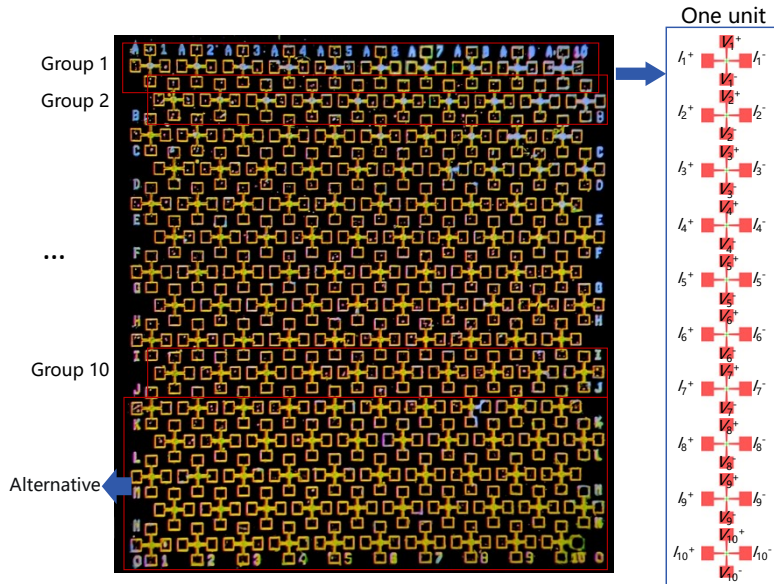


Fig. S6. Optical image of the fabricated PUF array showing 100 Hall bar devices, grouped into units of 10 devices each. Additionally, a schematic representation of the AHE measurements for each group of 10 devices is provided.

## S7: The bitmap and Hamming distances of negative currents for the first test

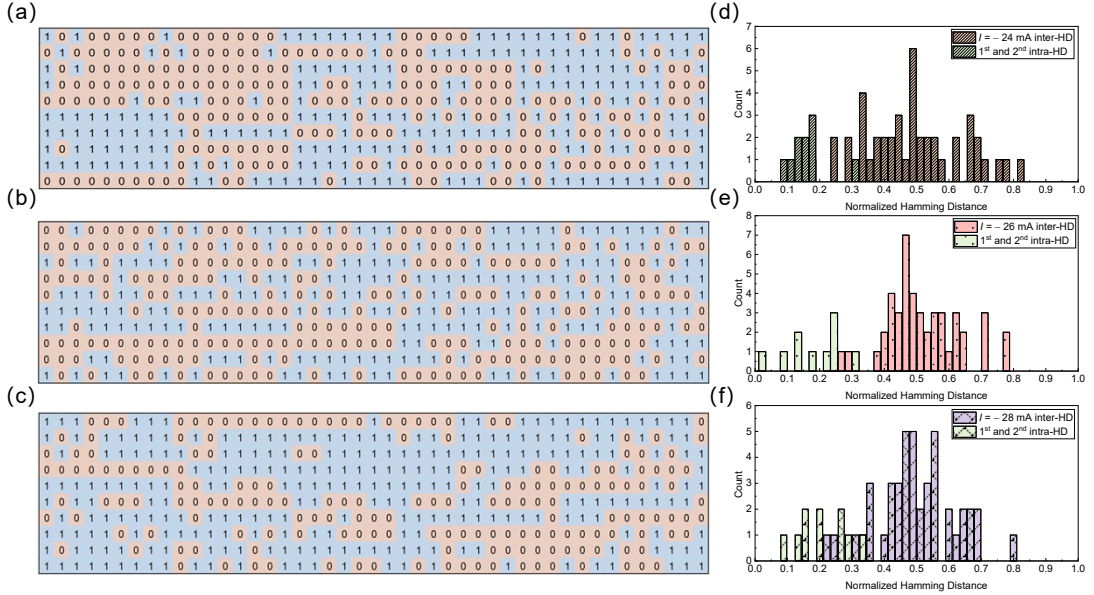


Fig. S7. Bitmap representations of a  $10 \times 45$  array generated using different amplitudes of negative pulse currents in the first test: (a) – 24 mA, (b) – 26 mA, and (c) – 28 mA. Additionally, the corresponding inter-Hamming and intra-Hamming distances for each of these amplitudes, (d) – 24 mA, (e) – 26 mA, and (f) – 28 mA.

## S8: Difference between multi-PUFs driven by SOT currents

To assess the irreproducible characteristic of multi-PUFs under varying amplitudes of pulse current, we computed the inter-Hamming distance among the writing currents. The initial test and comparison, illustrated in Figs. S8(a) - (f), as well as the subsequent test depicted in Figs. S8(g) - (i), revealed that the majority of mean inter-Hamming distance values are close to 0.5. This indicates a significant divergence between the writing currents.

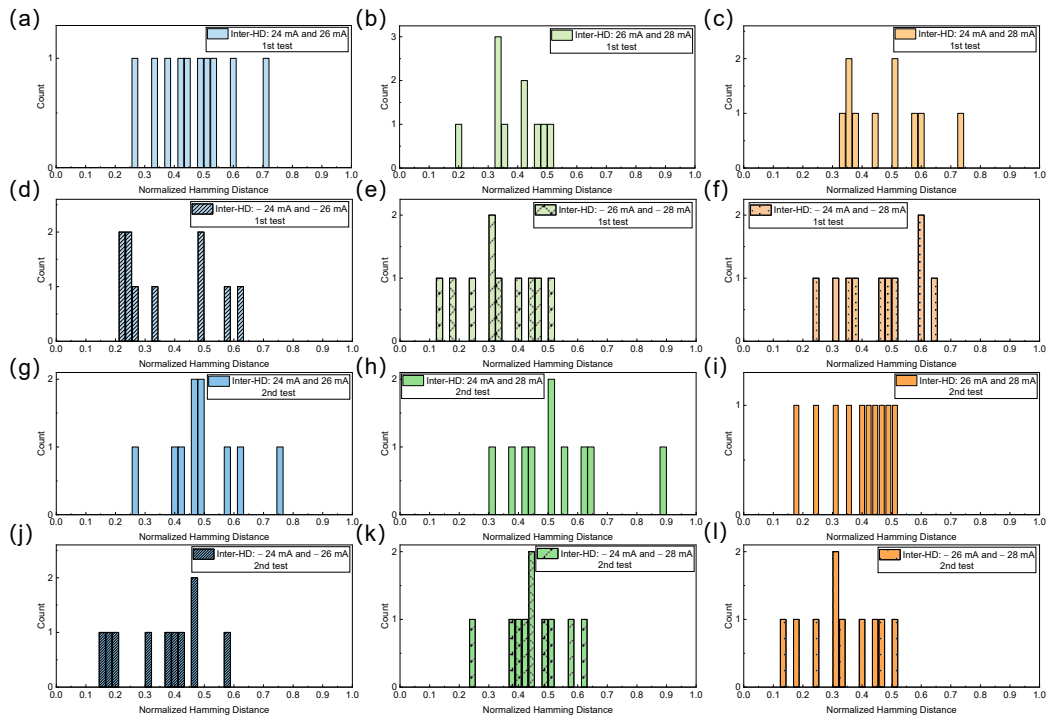


Fig. S8. The inter-Hamming distances between different writing currents for the first test: (a) - (f), and for the second test: (g) - (i).

Table S1: The mean value of the inter-Hamming distances between different writing currents for the first and second tests

Comparison samples	Mean value	
	The first test	The second test
24mA/26mA	0.46889	0.49556
24mA/28mA	0.48000	0.53086
26mA/28mA	0.38667	0.38222
-24mA/-26mA	0.37111	0.34321
-24mA/-28mA	0.46000	0.45333
-26mA/-28mA	0.33333	0.33333

## S9: The bitmap and Hamming distances of positive currents for the second test

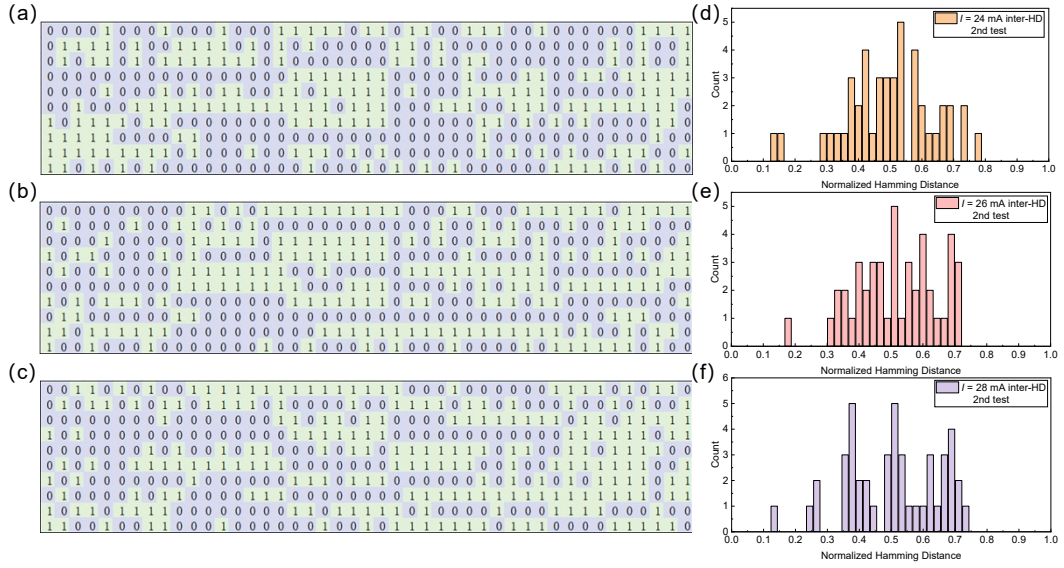


Fig. S9. Bitmap representations of a  $10 \times 45$  array generated using different amplitudes of positive pulse currents in the second test: (a) 24 mA, (b) 26 mA, and (c) 28 mA. Additionally, the corresponding inter-Hamming for each of these amplitudes, (d) 24 mA, (e) 26 mA, and (f) 28 mA.

## S10: The bitmap and Hamming distances of negative currents for the second test

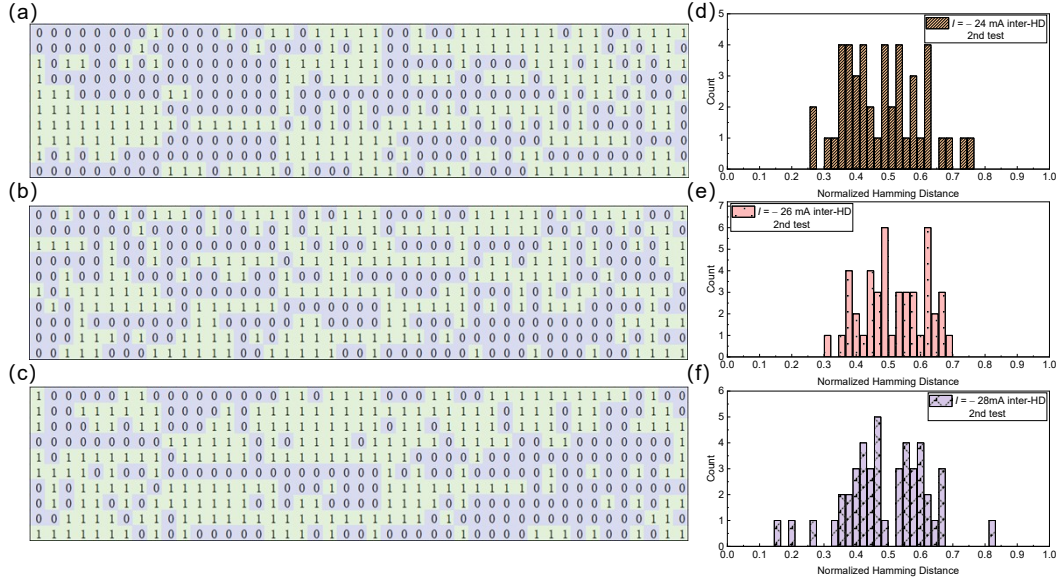


Fig. S10. Bitmap representations of a  $10 \times 45$  array generated using different amplitudes of negative pulse currents in the second test: (a)  $-24\text{ mA}$ , (b)  $-26\text{ mA}$ , and (c)  $-28\text{ mA}$ . Additionally, the corresponding inter-Hamming for each of these amplitudes, (d)  $-24\text{ mA}$ , (e)  $-26\text{ mA}$ , and (f)  $-28\text{ mA}$ .

Table S2: The mean and variance values of the inter-Hamming distances at different writing currents  
for the first and second tests

The applied pulsed current	The first test		The second test	
	Mean	Variance	Mean	Variance
24 mA	0.496	0.0136	0.4999	0.0199
26 mA	0.499	0.0126	0.517	0.0162
28 mA	0.472	0.0132	0.505	0.0213
- 24 mA	0.486	0.0237	0.482	0.0146
- 26 mA	0.520	0.0130	0.518	0.0098
- 28 mA	0.493	0.0162	0.492	0.0168

## Reference

- [1] A. Vansteenkiste, J. Leliaert, M. Dvornik, M. Helsen, F. Garcia-Sanchez, B. Van Waeyenberge, *AIP. Adv.* 2014, **4**, 107133.